LARGE-EDDY SIMULATIONS OF TURBULENT COMPRESSIBLE SUPERSONIC JET FLOWS USING DISCONTINUOUS GALERKIN METHODS

Diego F. Abreu[1,†,*]**, Carlos Junqueira-Junior**[2]**, Eron T. V. Dauricio**[1,‡] **and João Luiz F. Azevedo**[3]

[1] Instituto Tecnológico de Aeronáutica, 12228–900, São José dos Campos, SP, Brazil,
[†]mecabreu@yahoo.com.br , [‡]eron.tiago90@gmail.com

[2] Arts et Métiers Institute of Technology, DynFluid, CNAM, HESAM University, 151 Boulevard de l'Hôpital, 75013, Paris, France, junior.junqueira@ensam.eu

[3] Instituto de Aeronáutica e Espaço, 12228–904, São José dos Campos, SP, Brazil,
joaoluiz.azevedo@gmail.com

Key words: Large-Eddy Simulation, Turbulent Flow, Jet Flow, Discontinuous Galerkin Methods

Abstract. In this work, a discontinuous Galerkin scheme is employed to perform large-eddy simulations of supersonic jet flows. A total of four simulations are performed with different meshes and order of accuracy to identify the resolution requirements to reproduce the physical characteristics from experiments. The number of degrees of freedom from the simulations varies from 50×10^6 to 400×10^6. The results indicate that by increasing the resolution of simulation, in general, the results got closer to experimental data. The comparison of velocity distribution in the jet centerline and lipline from the simulation with 400×10^6 with experimental shows that important characteristics of the flow are represented. The study investigated a procedure of using lower-order simulations to initialize high-order simulations to reduce the total computational cost of the calculation. This strategy is successful and allows the performance of high-order simulations with only 6% more computational effort than a second-order simulation with the same number of degrees of freedom.

1 INTRODUCTION

The use of Reynolds-Averaged Navier-Stokes (RANS) formulation can be challenging when representing some types of fluid motions predominantly governed by free shear flows or wall-bounded flows with separated boundary layers. This difficulty is related to constructive assumptions of the formulation, characterized by the modeling of all turbulent quantities. The recent progress of computational power enables the employment of large-eddy simulations (LES) to simulate the problems that RANS formulation fails to model important aspects of the flow. Recent studies show the capability of LES simulations for reproducing free shear layer [5, 21] and detached flows [13, 22]. Another advantage of using LES is its capability to produce high-frequency unsteady information, which is necessary for aerodynamics, acoustics, loads, and heat transfer analyses.

1

The authors are interested in the simulation of supersonic jet flows for aerodynamic analyses of the shear layer regarding velocity and pressure fluctuations. Different numerical options are employed to obtain the solution of LES formulation for jet flows [18, 3, 9, 23, 4]. The discontinuous Galerkin formulation [15] presents some characteristics that are favorable for the conduct of LES calculations. The computation of the solution in each cell demands little information from the neighbors and the schemes permit the usage of numerical meshes with localized refinement, which is an advatage for jet flow calculations. These two characteristics provide high efficiency when performing parallel simulations. One can find in the literature jet flow simulations using discontinuous Galerkin schemes [1, 8].

The discontinuous Galerkin schemes have multiple options for implementation. One set of choices for the discontinuous Galerkin schemes is named discontinuous Galerkin spectral element method (DGSEM) [19, 16]. Such an approach is implemented in a numerical framework called FLEXI [20] which is evaluated in the present work. A resolution study is performed for LES of a supersonic round jet flow with Mach number equal to 1.4 and Reynolds number based on jet inlet diameter of 1.58×10^6.

In this work, the authors investigate the resolution requirements for the LES simulations to capture the characteristics of the jet flows presented in the physical experiments [6]. Three numerical meshes are utilized in the work. The first two meshes are designed to provide the same number of degrees of freedom (DOF) when simulated with two different polynomial orders for spatial for the numerical solution. The third mesh presents a higher refinement level in the region of the jet lipline and the region close to the jet inlet boundary condition and it presents a larger quantity of elements when compared to the first two meshes. The third mesh is simulated with first and second-order polynomials to investigate the influence of mesh and polynomial (hp) refinement. The number of DOFs from numerical simulation varies from 50×10^6 to 400×10^6. The results from the simulations are compared with the experimental data. A discussion on computational effort utilizing discontinuous Galerkin methods is also performed to develop guidelines for future work.

2 NUMERICAL FORMULATION

The work has an interest in the solution of the large-eddy simulation formulation. The approach is based on a spatial filtering process that separates the flow into a resolved part and a non-resolved part . An implicit filter is applied in which its size is obtained from the mesh size. The set of equations in its conservative form is presented in previous work [1]. The classic Smagorinsky model [25] is utilized to calculate the subgrid-scale contribution.

The nodal discontinuous Galerkin method is implemented in the computational framework called FLEXI [20]. In the DGSEM scheme, the domain is divided into multiple hexahedral elements. This choice of elements permits the interpolating polynomial to be defined as a tensor product basis with degree N in each space direction. This set of options leads to an algorithm with fewer complexity when compared to other schemes and also produce a high level of computational efficiency due to reduced calculations.

The numerical scheme used in the simulation additionally presents the split formulation [24], with the discrete form [11], to enhance the stability of the simulation. The split formulation is employed for Euler fluxes only. The solution and the fluxes are interpolated and integrated

at the nodes of a Gauss-Lobatto Legende quadrature, which presents the summation-by-parts property, that is necessary to employ the split formulation.

The Riemann solver used in the simulations is a Roe scheme with entropy fix [14] to ensure that the second law of thermodynamics is respected, even with the split formulation. For the viscous flux, the lifting scheme of Bassi and Rebay (BR2) [2] is used. The time marching method chosen is a five-stage, fourth-order explicit Runge-Kutta scheme [7]. The shock waves that appear in the simulation are stabilized using the finite-volume sub-cell shock-capturing method [26]. The shock indicator of Jameson, Schmidt and Turkel [17] is utilized.

3   NUMERICAL SETUP

In this work, the interest is to simulate the fully expanded free jet flow configuration with a Mach number of 1.4. In this configuration the jet flow has a static pressure in the nozzle exit section that equals the ambient static pressure with a supersonic velocity, for this reason, it is possible to avoid the use of nozzle wall geometries and also the shock waves are weaker when compared to other operating conditions. The experimental apparatus for the analyzed configuration is composed of a convergent-divergent nozzle designed with the method of characteristics [6] that produces a supersonic jet flow with a Reynolds number based on nozzle exit diameter of approximately 1.58×10^6.

3.1   GEOMETRY AND MESH CONFIGURATION

The geometry used for the calculations in the work presents a divergent shape and axis length of $40D$, where D is the jet inlet diameter and has external diameters of $16D$ and $25D$. Figure 1 illustrates a 2-D representation of the computational domain indicating the inlet surface in red, the far-field region in blue, the lipline in the gray line, the centerline in black, and the sponge zone represented by the gray region around the geometry.
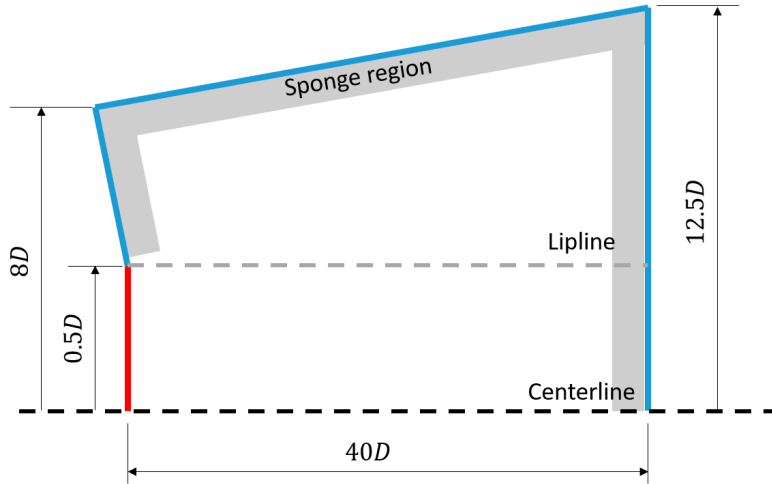
Figure 1: 2-D schematic representation of the computational domain used on the jet flow simulations.

The computational grids used in the work are named M-1, M-2, and M-3. The M-1 and M-2 meshes are adaptations of the mesh utilized in previous work [18] due to the different restrictions of each computational code. The M-3 mesh is generated with topological differences from M-1 and M-2 meshes. The M-3 mesh topology presents a high refinement level around the jet inlet boundary external diameter that transitions to a uniform distribution when moving forward in the longitudinal direction. In addition to the new topology, the M-3 mesh also presents a larger number of elements. Figure 2 exhibits a cut plane of the meshes utilized in the work. The M-1 and M-2 meshes have a total of 6.2×10^6 and 1.8×10^6 elements. The M-3 mesh has 15.4×10^6 elements. All the meshes utilized in the work are generated with the GMSH [12] generator. A summary of mesh information is provided in Table 1.

(a) M-1 mesh.

(b) M-2 mesh.

(c) M-3 mesh.
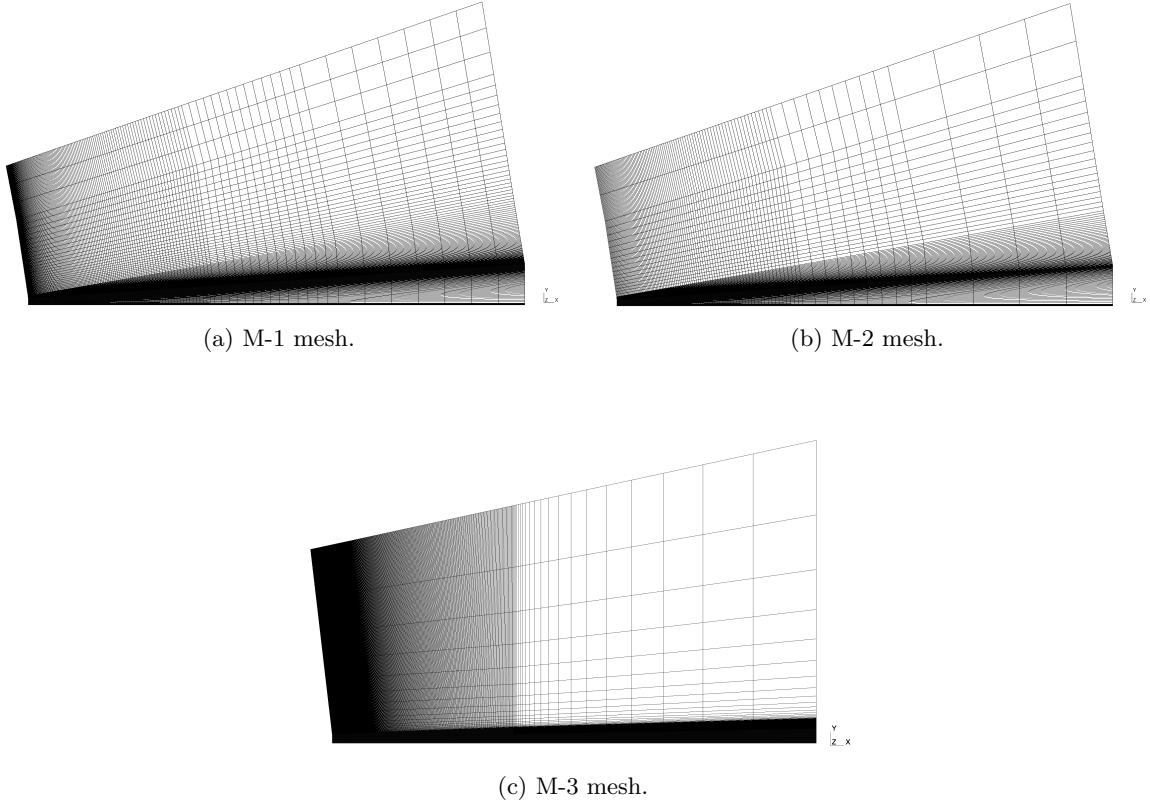
Figure 2: Visualization of the half-plane longitudinal cut planes for the meshes used in the present work.

3.2 BOUNDARY CONDITIONS

The reference states to characterize the jet inflow, $(\cdot)_{jet}$, and the far-field, $(\cdot)_{ff}$, indicated in Fig. 1 in red and blue, respectively. A weakly enforced solution of a Riemann problem with a Dirichlet condition is enforced at the boundaries. The flow is characterized as perfectly expanded with the same temperature of the free stream, i.e. $p_{jet}/p_{ff} = T_{jet}/T_{ff} = 1$, where p stands for

Table 1: Summary of simulations settings.

Simulation	Meshes	Order of Accuracy	DOF/cell	Cells (10^6)	Total # of DOF (10^6)
S-1	M-1	2nd order	8	6.2	≈ 50
S-2	M-2	3rd order	27	1.8	≈ 50
S-3	M-3	2nd order	8	15.4	≈ 120
S-4	M-3	3rd order	27	15.4	≈ 410

pressure and T for temperature. The Mach number of the jet at the inlet is $M_{jet} = 1.4$ and the Reynolds number based on the diameter of the nozzle is $Re_{jet} = 1.58 \times 10^6$. A small velocity component with $M_{ff} = 0.01$ in the streamwise direction is imposed at the far-field to avoid numerical issues. A sponge zone [10] is employed close to all far-field boundaries to dump any oscillation that could reach the boundaries, indicated in Fig. 1.

3.3 SIMULATION SETTINGS

A total of 4 simulations are compared in this work. The development of the simulations utilized 3 different meshes with two options of polynomial degree, which results in simulations with second-order and third-order accurate spatial discretizations. The S-1 simulation utilizes the M-1 mesh with a first-order polynomial. The S-2 simulation utilizes the M-2 mesh with a second-order polynomial. The S-3 and S-4 simulations utilize the M-3 mesh with first and second-order polynomials, respectively. Table 1 summarizes the simulations performed with the spatial order of accuracy and the total number of degrees of freedom.

3.4 CALCULATION OF STATISTICAL PROPERTIES

Two different approaches are taken to perform the 4 simulations. In the first approach, utilized for S-1, S-2, and S-3 simulations, the procedure involves three steps. The first one is to clean off the domain since the computation starts with a quiescent flow initial condition. The simulations run three flow-through times (FTT) to develop the jet flow. One FTT is the time required for one particle with the jet velocity to cross the computational domain. In the sequence, the simulations run an additional three FTT to produce a statistically steady condition. Then, in the last step, data are collected with a sample of approximately 250 kHz for another FTT to obtain the statistical properties of the flow. In the second approach, utilized for the S-4 simulation, the solution obtained from the S-3 simulation is utilized as the initial condition. The simulation is performed for 0.5 FTT to clean the second-order accuracy solution and allow it to provide a third-order accuracy solution. Then 2 additional FTT are simulated to extract data for the analysis.

The mean and the root mean square (RMS) fluctuations of properties of the flow are calculated along the centerline, lipline, and different domain surfaces in the streamwise direction. The centerline is defined as the line in the center of the geometry $y/D = 0$, whereas the lipline is a surface parallel to the centerline and located at the nozzle diameter, $y/D = 0.5$. The results from the lipline are an azimuthal mean from six equally spaced positions. The four surfaces in the streamwise positions are $x/D = 2.5$, $x/D = 5.0$, $x/D = 10.0$, and $x/D = 15.0$. Fig. 3

illustrates a snapshot of the jet flow with the lines and surfaces of data extraction. Mach number contours are presented in the figure.
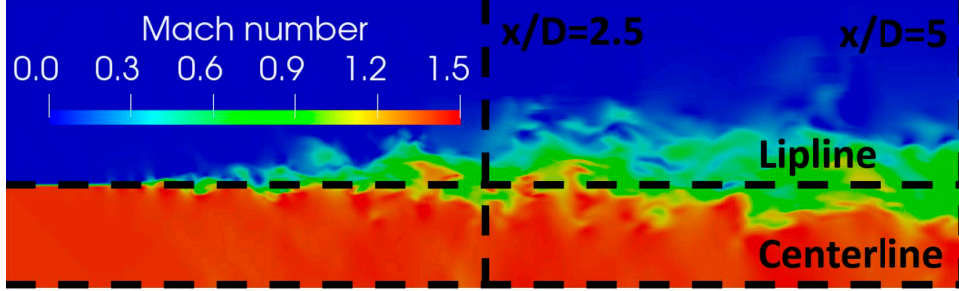
Figure 3: Snapshot of the jet simulation with the two longitudinal lines and three crossflow lines along which data is extracted. Mach number contours are shown.

4 RESULTS

4.1 ANALYSIS OF NUMERICAL RESULTS

The results from S1, S2, S3, and S4 simulations are presented in this section, which is divided into two parts. In the first one, contours of mean longitudinal velocity, RMS longitudinal velocity fluctuation, and mean density are presented for each simulation. In the second one, the distribution of mean longitudinal velocity and RMS of longitudinal velocity fluctuation are presented along the jet centerline and lipline for the four simulations and compared to experimental data. In the last set of qualitative results, the mean longitudinal velocity, RMS of longitudinal velocity fluctuation, RMS of radial velocity fluctuation, and shear-stress tensor are presented in four spanwise lines for all the simulations and compared to experimental data.

In the first part, three main aspects can be observed from the different variable contours. Each variable contours is best suited to investigate one of the three aspects. The length of the potential core, which is the length from the jet inlet condition that, in the centerline, the jet velocity reaches 0.95% of jet inlet velocity, cannot be directly assessed from visual inspection. However, the region with red contours represents the region with the highest jet velocity. One aspect that can be qualitatively assessed is the increment of the red contours region, which is related to an increment in the jet potential core length. The development of the shear layer can be visualized in all of the contours, however, the RMS of longitudinal velocity fluctuation is well suited to observe the shear layer. The last aspect that can be assessed from the contours is the development of the series of shock and expansion waves in the early stages of the jet.

Figure 4 presents the contours for the mean longitudinal velocity for all simulations. In Figs. 4a and 4b the contours of velocity are very similar. Analyzing the velocity contours in Fig. 4c, one can observe that the red region has a longer length when compared to previous contours, which is directly associated with the longer potential core of the jets. The improvement in the results obtained shows the importance of distributing elements where they are necessary. Finally, in Fig. 4d, the velocity contours from S4 simulation are presented. It is possible to observe that the red region is the longest among all the simulations, which may be indicative

that it was lacking resolution in previous simulations to adequately capture the development of the jet flow.

(a) S1 simulation.

(b) S2 simulation.

(c) S3 simulation.

(d) S4 simulation.
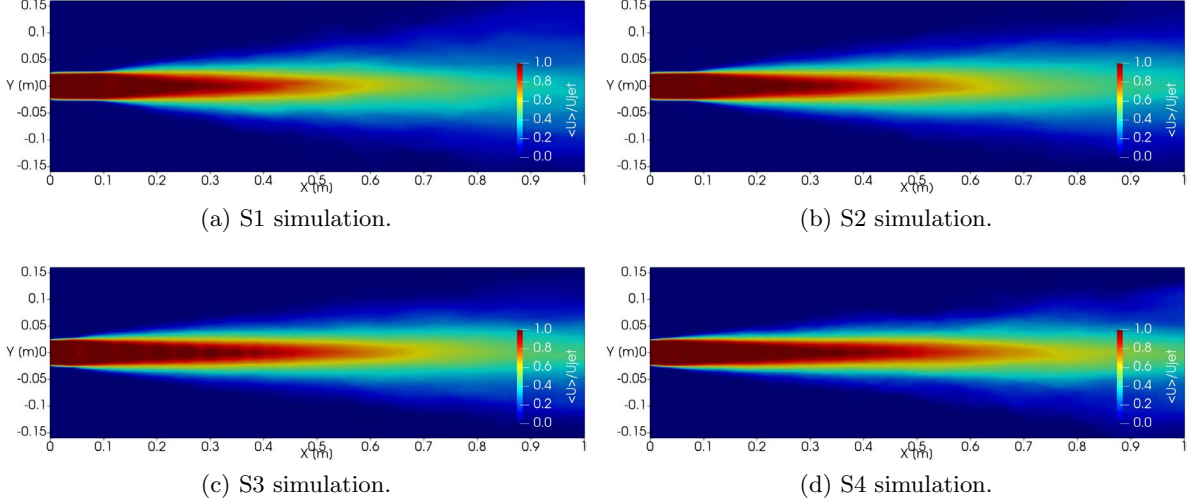
Figure 4: Contours of mean longitudinal velocity component on cutplane in $z/D = 0$.

Figure 5 presents the contours of RMS of longitudinal velocity fluctuation. The contours of velocity fluctuation presented in Figs. 5a and 5b from S1 and S2 indicate that the shear layer development is starting approximately $1D$ far from the jet inlet section. Just after the initial development of the shear layer development, one can observe that the peak of RMS fluctuation occurs, which can be associated with the large difference between the velocities and possibly the transition of the shear layer from laminar to turbulent. The velocity fluctuation contours presented in Fig. 5c from the S3 simulation have significant differences from the two previously discussed. The development of the shear layer is starting closer to the jet inlet section with smaller peaks of RMS of velocity fluctuation. One can visualize that the two mixing layers are crossing in the center of the jet farther in Fig. 5c than in Figs. 5a and 5b even presenting a sooner development, which can be an indication of smaller spanwise spreading of velocity fluctuation. Analyzing the velocity contours in Fig. 5d, one can observe that the tendencies from the comparison of S3 simulation with S1 and S2 are present with larger intensities, which means that the beginning of the development of the shear layer got closer to the jet inlet section and the crossing of the two mixing layers is happening farther from jet inlet section when comparing to the velocity fluctuation contours from S3 simulation, Fig. 5c. The velocity fluctuation contour, from the S4 simulation, Fig. 5d, is the one with smaller spreading and early development of the shear layer among all the simulations.

Finally, in Fig. 6, the contours of mean density are presented for all simulations. In these figures, it is possible to better visualize the development of the series of shocks and expansion waves. Different from what has been observed in Figs. 4 and 5, one can observe differences regarding the series of shock and expansion waves between the density contours from S1 and S2 simulation, in Figs. 6a and 6b. In Fig. 6a only three sets of shocks and expansion waves are visible, while in Fig. 6b it is possible to observe more than 6 sets. It is possible to observe

(a) S1 simulation.

(b) S2 simulation.

(c) S3 simulation.
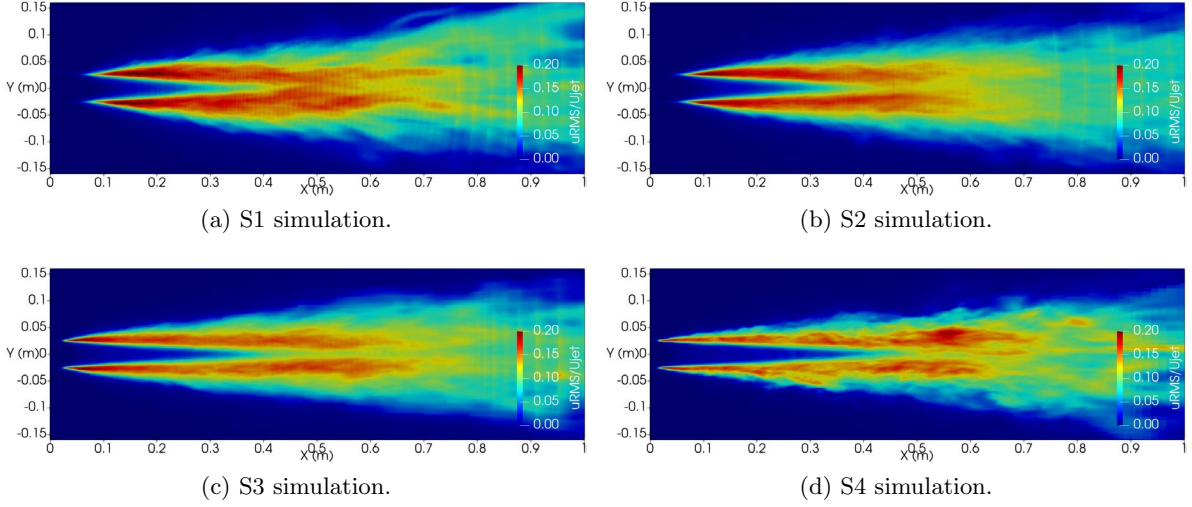
(d) S4 simulation.

Figure 5: Contours of RMS of longitudinal velocity fluctuation on cutplane in $z/D = 0$.

also that the sets of shocks and expansion waves from the S2 simulation are stronger than those from the S1 simulation. Analyzing Fig. 6c, it is possible to observe that the S3 simulation produced even more sets of shocks and expansion waves than the S2 simulation, Fig. 6b, with stronger shock waves, that are evaluated by the higher values of mean density presented in the mean density contours. Another aspect that can be observed is that the first set of shock and expansion waves in the S3 simulation is occurring closer to the jet inlet section than in S2 and S1 simulations, and it appears to be a correlation between the first set of shock and expansion waves with the beginning of the development of the shear layer. In Fig. 6d the density contours from S4 simulation is presented. One can observe the largest set of shock and expansion waves among all the simulations and also a thinner representation of the shocks and expansion waves, which can be closely associated with the increased resolution of the simulation. It is also possible to observe a reduction in the strength of the sets of shock and expansion waves when compared to the S3 simulation, Fig. 6c.

Figure 7 presents the numerical results of velocity from all simulations compared to the experimental data [6]. In Fig. 7a, the distribution of mean longitudinal velocity $< U > /U_j$ is presented along the centerline of the jet. One can observe in the figure that the mean velocity profiles from S1 and S2 simulations are almost equal. The velocity distribution from the S3 simulation presents a significant improvement when compared to previously performed simulations and the S4 simulation could almost capture the shape of the velocity distribution observed in the experiments. In Fig. 7b the RMS of longitudinal velocity fluctuation u_{rms}/U_j is presented along the centerline of the jet. It is possible to observe in the RMS of velocity fluctuation the positive influence of the increased resolution on the numerical results regarding the proximity to experimental data. The differences between S1 and S2 simulations are small, the S3 simulation got closer to experimental data and the S4 simulation once more presented the best match with experimental data. It can be observed in Fig. 7b from the S4 simulation a double peak that does not appear in any other simulation or the experimental data. This behavior may be related

(a) S1 simulation.

(b) S2 simulation.

(c) S3 simulation.

(d) S4 simulation.
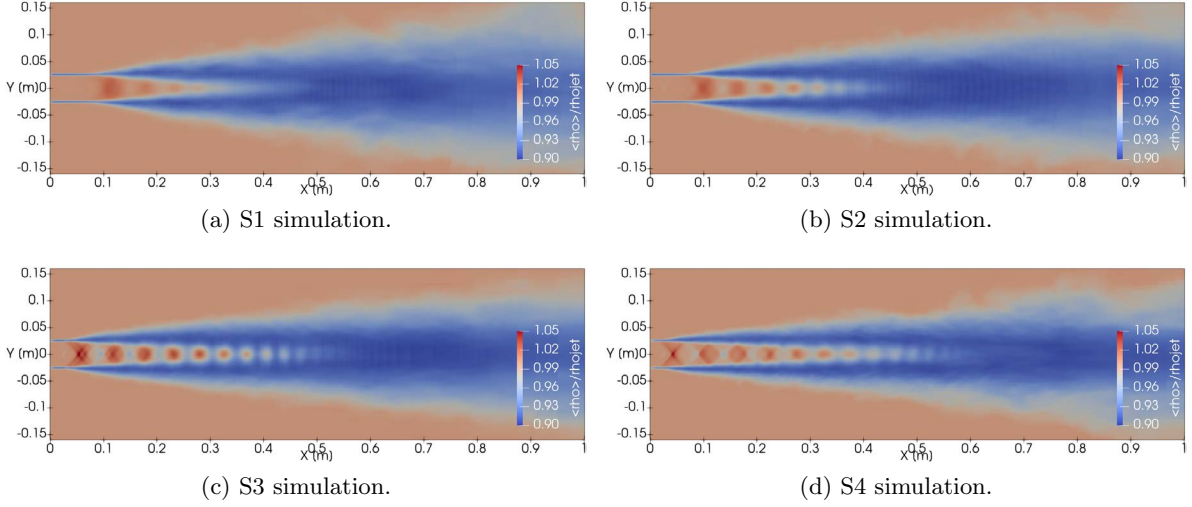
Figure 6: Contours of mean density on cutplane in $z/D = 0$.

to the lack of data acquisition for the calculation of statistical properties. Since the goal of the paper is to study the effects of resolution on the calculation, the authors do not intend to use computational resources to match the simulation results with the experimental data. However, for future and more realistic numerical calculations one shall considering improvements on data extraction for statistical purposes.

While the velocity distribution in the jet centerline present always improvements in the simulations with increased resolution, in the lipline that behavior is not observed. In Fig. 7c, where the mean longitudinal velocity $< U > /U_j$ is presented in the lipline of the jet, one may observe that far from the jet inlet section, the increased resolution produced improvements in the velocity distribution, which is not observed close to the jet inlet boundary condition. When analyzing the distribution of the RMS of longitudinal velocity distribution along the lipline of the jet, Fig. 7d, one can observe that the increased resolution pushed the profiles of velocity distribution away from experimental data. While in the experimental data it is possible to observe a smooth growth of RMS of longitudinal velocity fluctuation and almost a plateau from $x/D = 5$ to $x/D = 15$, in all the simulations there is a sudden increase in the RMS of longitudinal velocity fluctuation and after the peak, a constant reduction on the values is observed. The differences observed in these results may be related to the choice of the boundary condition imposed for the jet inlet that does not represent the physical characteristics of the experiments.

The results in Fig. 8 present different statistical properties of the flow in different longitudinal positions. The first set of results, in Figs. 8a to 8d, concerns the mean of longitudinal velocity. The S1 simulation is in agreement with the experimental data at $x/D = 2.5$, Fig. 8a. In the position $x/D = 5$, Fig. 8b all the simulations produce very similar results. Moving forward and analyzing data in position $x/D = 10$, Fig. 8c it is possible to observe a similar behavior between S1 and S2 simulations, S3 simulation presenting improvements to the other two and S4 simulation presenting the best match with experimental data. In the last position $x/D = 15$,

(a) Centerline

(b) Centerline
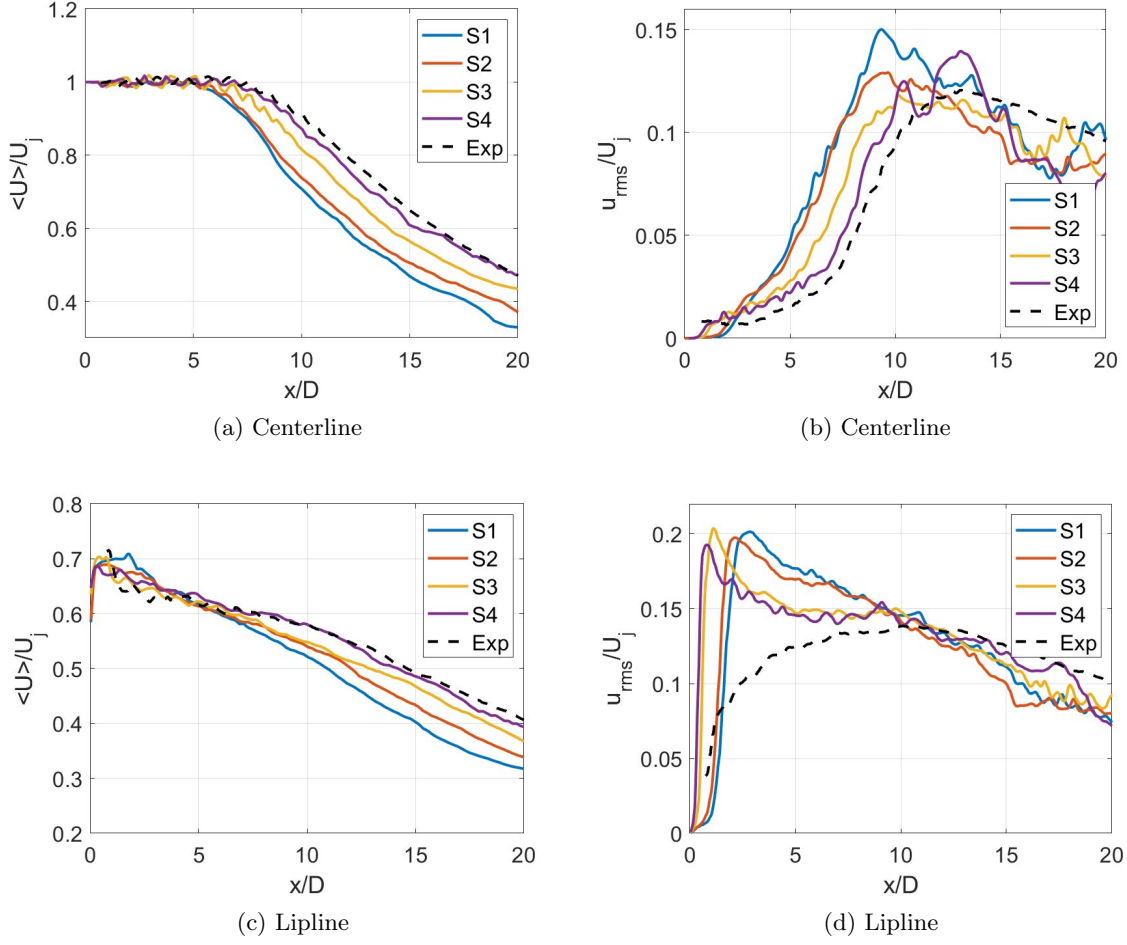
(c) Lipline

(d) Lipline

Figure 7: Results of mean streamwise velocity component distribution (left) and RMS of stream-wise velocity fluctuation (right) in the jet centerline $y/D = 0$ (top) and lipline $y/D = 0.5$ (bottom).

Fig. 8a, improvements are observed with increased resolution of the simulations.

The profiles of RMS values of longitudinal velocity fluctuation are presented in Figs. 8e to 8h. The simulation profiles at $x/D = 2.5$, Fig. 8e, present a similar shape between themselves with differences only in the value of the peak of RMS of longitudinal velocity fluctuation. The increased resolution of the simulation produces smaller values in the peak of velocity fluctuation, getting closer to experimental data. A similar shape of the profiles is observed in the next position at $x/D = 5$, Fig. 8f. In the position $x/D = 10$, Fig. 8g the main aspects of the flow are captured, except for higher values of RMS of longitudinal velocity fluctuation in the center of the jet. The velocity fluctuation profiles for all simulations and experimental data are very similar in the last position $x/D = 15$, Fig. 8h.
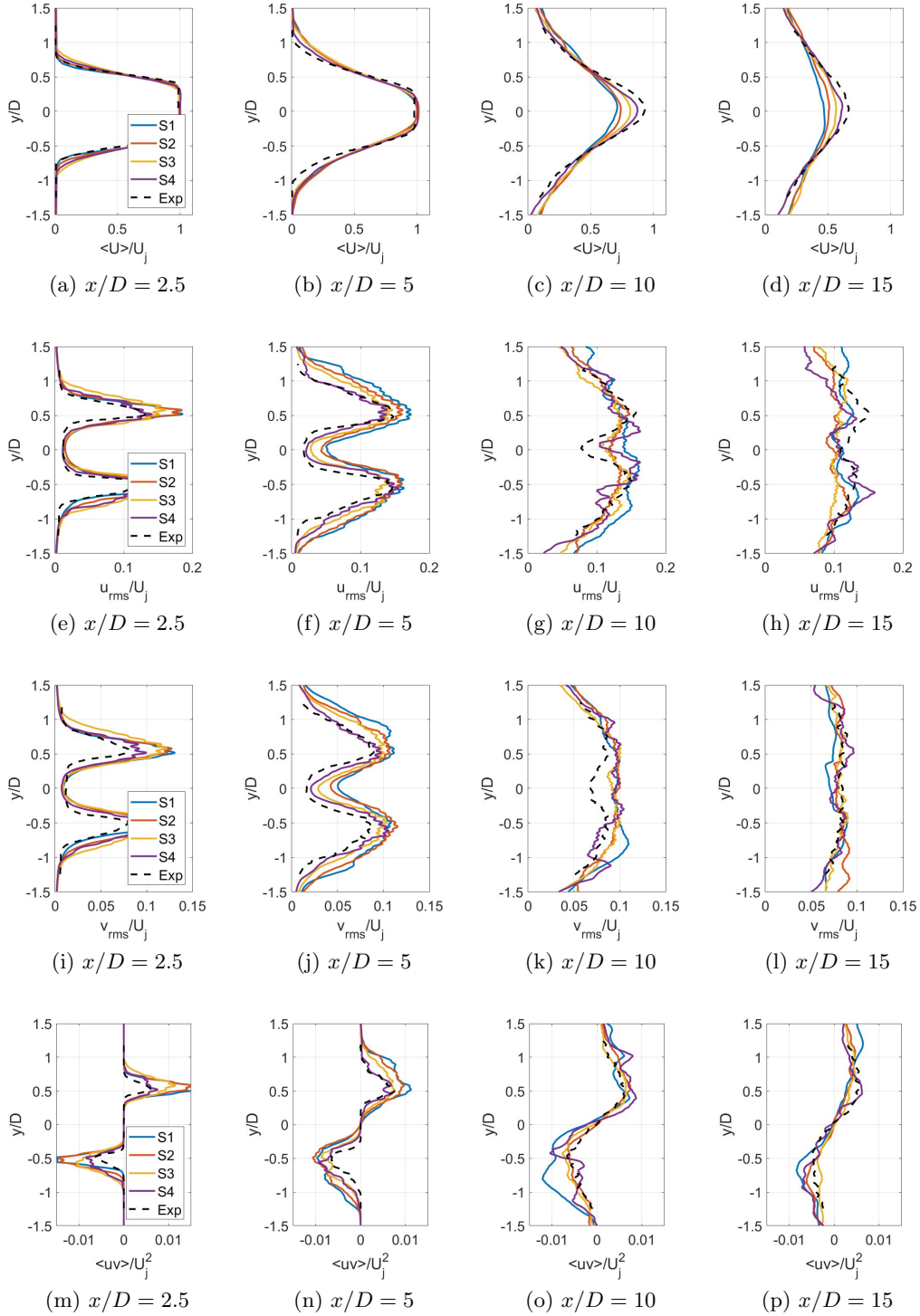
Figure 8: Profiles of mean streamwise velocity component, RMS of streamwise velocity fluctuation, RMS of radial velocity fluctuation, and mean shear-stress tensor component (from top to bottom) at four streamwise positions $x/D = 2.5$, $x/D = 5$, $x/D = 10$ and $x/D = 15$ (from left to right).

11

Profiles of RMS values of radial velocity component fluctuation are presented in Figs. 8i to 8l. They exhibit similar shapes when compared to the profiles of the longitudinal velocity fluctuation, Figs. 8e to 8h. One can also observe the positive effects of the increased resolution on the profiles of the mean shear-stress tensor component, Figs. 8m to 8p. The profiles from the S4 simulation are in good agreement with the experimental data, due to the closeness between the values of shear-stress tensor, and they indicate considerable improvement when compared to the simulations with smaller resolution.

The simulation results make it possible to observe, in general, that the improved resolution of the simulations produced better results compared to experimental data. The simulation with the highest resolution, the S4 simulation, is the one that better matches the experimental data. Due to the closeness between the numerical results from S4 simulation with experimental data, the authors have evidence that the resolution requirements for performing supersonic jet flow simulation with analyzed operating conditions are well suited for future calculations considering another jet flow configuration. It is possible to observe some differences between the numerical results from all simulations with experimental data along the lipline of the nozzle, which may be associated with the fact that the jet inlet boundary condition does not represent the characteristics of the flow from physical experiments. The continuity of the work focuses on strategies to reproduce a jet inlet condition that better represents the physical flow.

4.2   ANALYSIS OF COMPUTATIONAL EFFORT

The present section discuss aspects of computational effort to be able to reduce costs of the simulations. The main parameter utilized to measure the efficiency of a simulation is the Performance Index PID, which can be calculated by

$$PID = \frac{wall\ clock\ time\ n_{cores}}{n_{DOF}\ n_{\Delta t}\ n_{RK-stages}}, \tag{1}$$

where *wall clock time* is the time the simulation needed to perform $n_{\Delta t}$ time steps, n_{cores} is the quantity of cores used in the simulation, n_{DOF} is the number of DOF of the simulation and $n_{RK-stages}$ is the number of stages from the Runge-Kutta scheme. The PID was calculated for all four simulations and the results are presented in Tab. 2.

Table 2: Summary of Performance Index PID from all simulations.

Simulation	PID (μs)
S1	8
S2	15
S3	5
S4	2

It is important to clarify to the reader that the numerical solver presented some improvements, associated with compiler optimization, during the execution of the simulations and they can be associated with the PID reduction from S3 and S4 simulations compared to S1 and S2 simulations. It is also possible to argue that, with the increased number of degrees of freedom, it is expected that more computation with a similar number of cores is performed, increasing the

ratio of computation to communication, which can reduce the total time of the simulations. If we compare only S1 and S2 simulations, for the same number of DOF, the third-order accurate simulations cost almost twice the effort of a second-order accurate simulation. If these values are employed in the two simulations procedure performed in this analysis, the total cost of the simulation can be compared.

The first simulation procedure involves the whole calculation of the 9 FTT with a mesh of 50×10^6 elements that produces $\approx 400 \times 10^6$ DOF when simulated with second-order accurate discretization, which could produce a similar result to those of S4 simulation. If the complete procedure for S4 simulation is performed, it could initially start its 5 FTT with second-order accurate discretization with a total of 120×10^6 DOF, then, the last 4 FTT are performed with a third-order accurate discretization with $\approx 400 \times 10^6$ DOF. If no influence on the computation to communication ratio is considered for the computational effort, the cost of the first stage of the simulation would be $3.34\times$ smaller than those to perform the first simulation procedure. Then the second stage of the simulation would cost twice those performed in procedure one. If the time to perform one FTT with second-order accurate simulation and $\approx 400 \times 10^6$ DOF is 1 h, the total computational time is 9 h. For the second simulation procedure, the cost to perform the first stage is ≈ 1.5 h and the time to perform the second stage is 8 h. The total simulation procedure time is ≈ 9.5 h. The resultant computational time to perform the simulation using the second strategy would be $\approx 6\%$ larger than the procedure used in the first simulation procedure.

Once it is possible to start the high-order simulation with a previous result from another order of accuracy with the same mesh, it is possible to reduce the time required to obtain the desired data with high-order simulation and consequently reduce the cost of the total simulation. In the proposed procedure, the cost of the total third-order accurate simulation was only 6% larger than those of a second-order accurate simulation. This result is expressive and very interesting for high-order simulations. Another important point to present here is that the computational code utilized presented very good scalability. The tests for the S4 simulation varied the number of cores from a few hundred cores to a few thousand cores and the PID was always close to $2\mu s$.

5 CONCLUDING REMARKS

In this work, the employment of a discontinuous Galerkin framework called FLEXI was investigated for the LES simulation of supersonic free round jets to identify the resolution requirements to reproduce the characteristics of the flows obtained in physical experiments. A total of four simulations are performed with 3 different meshes and second and third-order accurate discretizations. The range of degrees of freedom from the simulations varies from 50×10^6 to 400×10^6. All the simulations are performed for the same geometric model and with the same boundary conditions.

The qualitative analysis of the simulations is firstly performed to compare how they are capturing the main features of the flow: extension of the potential core of the jets, development of the shear layer, and development of the sets of shocks and expansion waves. The contours of the variables showed that with increased resolution the potential core of the jet got longer. The development of the shear layer starts closer to the jet inlet section and presents a smaller spreading. The number of sets of shocks and expansion waves increased and the width of the shocks and expansion waves are thinner.

The quantitative analysis showed that, in general, the increase in the resolution of the simulation, especially the number of degrees of freedom, produced better results when compared to experimental data. This is observed in the results of mean longitudinal velocity distribution and RMS of longitudinal velocity fluctuation distribution in the centerline. It is also observed in the results from the four spanwise planes. The results of velocity distribution in the lipline presented some differences from the numerical data. The jet inlet boundary condition utilized of uniform velocity does not represent what is obtained in physical experiments and may be associated with the differences observed.

The analysis of the computational effort of the simulation showed that even utilizing a high-order method that costs more than a second-order method for the same number of degrees of freedom it was possible to reproduce a third-order simulation with only 6% more computational cost of total simulation by initializing the simulation with a smaller order of accuracy.

The work reached is objective of identifying the guidelines for performing LES simulations of supersonic jet flows using a discontinuous Galerkin scheme with adequate results with a reasonable computational cost. The open point on the jet inlet condition is the next step in the development of the work.

ACKNOWLEDGMENTS

REFERENCES

[1] Abreu, D. F., Junqueira-Junior, C., Dauricio, E. T. V., and Azevedo, J. L. F. A comparison of low and high-order methods for the simulation of supersonic jet flows. In Proceedings of the 26th ABCM International Congress of Mechanical Engineering, COBEM Paper No. 2021-0388, Florianópolis, Santa Catarina, Brazil, November (2021).

[2] Bassi, F. and Rebay, S. A high-order accurate discontinuous finite element method for the numerical solution of the compressible Navier-Stokes equations. *Journal of Computational Physics*, 131:267–279, (1997).

[3] Bogey, C. and Bailly, C. Influence of nozzle-exit boundary-layer conditions on the flow and acoustic fields of initially laminar jets. *Journal of Fluid Mechanics*, 663:507–538, (2010).

[4] Brès, G. A., Ham, F. E., Nichols, J. W., and Lele, S. K. Unstructured large-eddy simulations of supersonic jets. *AIAA Journal*, 55(4), Apr. (2017).

[5] Brès, G. A. and Lele, S. K. Modelling of jet noise: A perspective from large-eddy simulations. *Philosophical Transactions of the Royal Society A*, 377(2159):20190081, (2019).

[6] Bridges, J. and Wernet, M. P. Turbulence associated with broadband shock noise in hot jets. In 29th AIAA Aeroacoustics Conference, AIAA Paper No. 2008-2834, Vancouver, British Columbia, Canada, May (2008).

[7] Carpenter, M. H. and Kennedy, C. A. Fourt-order 2N-storage Runge-Kutta schemes. Technical Report NASA-TM-109112, NASA Langley Research Center, (1994).

[8] Corrigan, A., Kercher, A., Liu, J., and Kailasanath, K. Jet noise simulation using a higher-order discontinuous Galerkin method. In Proceedings of the 2018 AIAA Aerospace Sciences Meeting, AIAA Paper No. 2018-1247, Kissimmee, FL, January (2018).

[9] DeBonis, J. R. Prediction of turbulent temperature fluctuations in hot jets. In Proceedings of the 23th AIAA Computational Fluid Dynamics Conference, AIAA Paper No. 2017-0610, Denver, CO, June (2017).

[10] Flad, D. G., Frank, H. M., Beck, A. D., and Munz, C.-D. A discontinuous Galerkin spectral element method for the direct numerical simulation of aeroacoustics. In Proceedings of the 20th AIAA/CEAS Aeroacoustics Conference, AIAA Paper No. 2014-2740, Atlanta, GA, June (2014).

[11] Gassner, G. J., Winters, A. R., and Kopriva, D. A. Split form nodal discontinuous Galerkin schemes with summation-by-parts property for the compressible Euler equations. *Journal of Computational Physics*, 327:39–66, (2016).

[12] Geuzaine, C. and Remacle, G.-F. GMSH: A three-dimensional finite element mesh generator with built-in pre- and post-processing facilities. *International Journal for Numerical Methods in Engineering*, 79(11):1309–1331, (2009).

[13] Ghate, A. S., Gaetan, K. K., Stich, G.-D., Oliver, M. B., Jeffrey, A. H., and Kiris, C. C. Transonic lift and drag predictions using wall-modelled large eddy simulations. In AIAA Scitech 2021 Forum, AIAA Paper No. 2021-1439, Virtual event, January (2021).

[14] Harten, A. and Hyman, J. M. Self adjusting grid methods for one dimensional hyperbolic conservation laws. *Journal of Computational Physics*, 50:253–269, (1983).

[15] Hesthaven, J. S. and Warburton, T. *Nodal Discontinuous Galerkin Methods - Algorithms, Analysis, and Applications*. Springer, New York, 1st edition, (2008).

[16] Hindenlang, F., Gassner, G. J., Altmann, C., Beck, A. D., Staudenmaier, M., and Munz, C.-D. Explicit discontinuous Galerkin methods for unsteady problems. *Computer & Fluids*, 61:86–93, (2012).

[17] Jameson, A., Schmidt, W., and Turkel, E. Numerical solution of the Euler equations by finite volume methods using Runge-Kutta time-stepping schemes. In Proceedings of the AIAA 14th Fluid and Plasma Dynamic Conference, AIAA Paper No. 1981-1259, Palo Alto, CA, (1981).

[18] Junqueira-Junior, C., Yamouni, S., Azevedo, J. L. F., and Wolf, W. R. Influence of different subgrid-scale models in low-order LES of supersonic jet flows. *Journal of the Brazilian Society of Mechanical Sciences and Engineering*, 40:258.1–258.29, (2018).

[19] Kopriva, D. A. and Gassner, G. J. On the quadrature and weak form choices in collocation type discontinuous Galerkin spectral element methods. *Journal of Scientific Computing*, 44:136–155, (2010).

[20] Krais, N., Beck, A. D., Bolemann, T., Frank, H. M., Flad, D., Gassner, G. J., Hindenlang, F., Malte Hoffmann, M., Kuhn, T., Sonntag, M., and Munz, C.-D. FLEXI: A high order discontinuous Galerkin framework for hyperbolic–parabolic conservation laws. *Computers and Mathematics with Applications*, 81:186–219, (2021).

[21] Kumar, P. and Mahesh, K. Large eddy simulation of propeller wake instabilities. *Journal of Fluid Mechanics*, 814:361–396, (2017).

[22] Masoudi, E., Gan, L., and Sims-Williams, D. Large eddy simulation of incident flows around polygonal cylinders. *Physics of Fluids*, 33(10):105112, (2021).

[23] Mendez, S., Shoeybi, M., Sharma, A., Ham, F. E., Lele, S. K., and Moin, P. Large-eddy simulations of perfectly expanded supersonic jets using an unstructured solver. *AIAA Journal*, 50(5), May (2012).

[24] Pirozzoli, S. Numerical methods for high-speed flows. *Annual Review of Fluid Mechanics*, 43:163–194, (2011).

[25] Smagorinsky, J. General circulation experiments with the primitive equations: I. The basic experiment. *Monthly Weather Review*, 93(3):99–164, (1964).

[26] Sonntag, M. and Munz, C.-D. Efficient parallelization of a shock capturing for discontinuous Galerkin methods using finite volume sub-cells. *Journal of Scientific Computing*, 70:1262–1289, (2017).